Journal of Sound and Vibration (1999) **225**(2), 353–374
Article No. jsvi.1999.2284, available online at http://www.idealibrary.com on IDEAL®

SOUND RADIATION FROM PROPELLERS IN FORWARD FLIGHT

M. CARLEY

Department of Mechanical and Manufacturing Engineering, Trinity College, Dublin 2, Ireland

(*Received* 18 *November* 1998, *and in final form* 16 *April* 1999)

A method is presented for the exact numerical integration of acoustic radiation integrals for a disc-shaped source in a mean flow. The technique allows the calculation of a harmonic of the acoustic field around the source and the study of its variation with the parameters relevant to aircraft propeller noise. Results are given for two sources representative of "conventional" and "advanced" aircraft propellers at zero, takeoff and cruise Mach numbers. The structure of the fields is discussed and in particular the form of the transition from the near to the far field and the circumstances under which the strong beaming pattern of supersonic rotors becomes apparent.

1. INTRODUCTION

Calculation of the acoustic field radiated by rotating sources is a problem of interest in the prediction of noise from aircraft propellers and rotors. The main techniques for such noise prediction are based on the Ffowcs Williams–Hawkings equation [1] or the generalized treatment of Goldstein [2], an integral equation for the sound radiated by an aerodynamic source region to some observer position. For direct prediction of the time-record of the noise at a given point, the various formulations of Farassat and co-workers [3–5] are among the best known, while Hanson's methods have a similar importance for frequency-domain predictions [6–8]. These methods involve integration over the propeller blade surface and so have become feasible only as computing power has increased. They are unsuited to the twin problems of quickly generating approximate solutions for initial design and the investigation of the general properties of the whole acoustic field.

Over the recent years, a number of researchers have published methods, often based on asymptotic analysis, which have been useful both for approximate prediction and the study of the general properties of rotating sound fields. The asymptotic analyses have included the prediction methods of Parry and Crighton for subsonic [9] and supersonic [10] rotors, Prentice's study of energy transport in rotating fields [11] and Chapman's study of the acoustic field of a rapidly rotating source distribution [12]. This study was extended by Chapman [13] using a combined analytical and numerical method which allows an efficient, exact,

0022–460X/99/320353 + 22 $30.00/0

evaluation of the acoustic field. This increased efficiency makes it possible to calculate the radiated sound at a large number of points so that the general properties of the whole acoustic field can be calculated without recourse to the approximations previously used, such as those of large observer distance or high harmonic number. The form of transition from the acoustic near field to the far field is thus highlighted, as is the form of the acoustic field in different regions of space such as the "quiet zone" of supersonic rotors. The predictions thus act as confirmation of the results of the asymptotic theories and as a useful set of results in their own right. In this paper, one of the outstanding issues listed in reference [13], the effect of forward motion of the source, is considered. This allows the method to be useful in studying the structure of the sound fields radiated by propellers in flight, a problem of industrial as well as purely scientific interest.

2. CALCULATION OF RADIATED SOUND

In this section, integrals for the pressure field radiated by a translating propeller are derived. In the following section, a method is outlined for their efficient calculation, based on that of Chapman [13]. The propeller is modelled as a disc in the plane $z = 0$, of radius a, rotating with angular velocity Ω (Figure 1). The reduction of the propeller to a disc assumes that the blades extend much less than one acoustic wavelength along the propeller axis. This is a valid assumption for straight blades of acoustically compact cross-section. The extension to blades of non-compact axial extent would involve calculating interference effects between regions at different axial positions, which could be done using methods similar to those presented here. It is further assumed that the hub can be ignored. In a real propeller, the hub does not contribute to the radiated noise. Including this effect in the data to be presented here would require subtracting a scaled version of the acoustic field from the overall results. Since, the results are to be compared with the previous results of Chapman [13] and since it is known that the noise of propellers is dominated by the blade tip or by the sonic radius [9, 10], the hub has not been modelled in this work.

Cylindrical co-ordinates are used with the observer at a position (r, θ, z) and (r_1, θ_1) being the co-ordinates on the propeller disc. The flight Mach number is M_∞ and the propeller either advances at speed cM_∞ (the "moving propeller" case) or operates in an axial flow of this velocity ("moving medium"), where c is the speed of sound in the fluid. The observer is considered stationary in each case. The wave equation to be solved for the acoustic pressure p is [14, 15], neglecting non-linear terms,

$$\left(\frac{1}{c^2}\frac{\mathrm{D}^2}{\mathrm{D}t^2} - \nabla^2\right) p = \frac{\mathrm{D}}{\mathrm{D}t}\left[\rho v_n \delta(f)\right] - \nabla\left[\mathbf{l}\delta(f)\right], \tag{1}$$

$$\frac{\mathrm{D}}{\mathrm{D}t} = \frac{\partial}{\partial t} - cM_\infty \frac{\partial}{\partial z} \quad \text{(moving medium)},$$

$$\frac{\mathrm{D}}{\mathrm{D}t} = \frac{\partial}{\partial t} \quad \text{(moving propeller)},$$

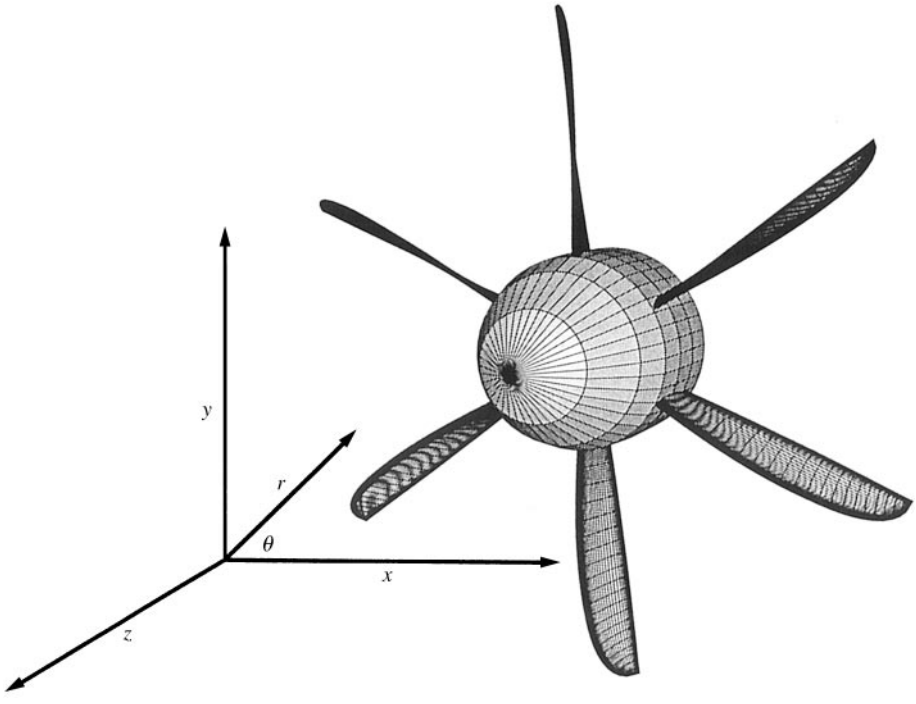

Figure 1. Propeller and observer co-ordinates.

with ρ being the undisturbed fluid density. The propeller blade surface is assumed symmetric and is specified by the function $f(\mathbf{x}) = 0$. The fluid velocity normal to the blade surface is v_n and the surface exerts a force **1** per unit area on the fluid. Since the propeller rotates at a constant velocity, the blade loading and geometry can be decomposed into Fourier series in θ_1 and the acoustic field due to each component calculated separately. The coefficients of the Fourier series for the geometry are denoted $\varepsilon a f_n(r_1)$ (with ε small) and the loading terms $g_n(r_1)$. The surface normal velocity v_n, required for the thickness noise calculation is then given by $v_n = -\mathrm{j}n\Omega f_n$. The blade loading is modelled as a unit pressure jump across the disc. For the sake of brevity, the blade drag noise is not included here although it could be calculated using the methods developed in this paper.

Two possible cases are considered in the calculations, the first being that of a propeller advancing in stationary fluid with sound being radiated to a stationary observer, the second where both propeller and observer are stationary in a uniform flow. The frequency-domain Green's function to be used in each case is that of Garrick and Watkins [16], which is, for a harmonic source $\exp(-\mathrm{j}\omega t)$,

$$G = \frac{\mathrm{e}^{\mathrm{j}k\sigma}}{4\pi S}, \quad \text{with } k = \omega/c. \tag{2}$$

The phase and amplitude radii σ and S have different definitions depending on whether the source is advancing or is stationary in a uniform flow. In the case of

a source advancing into quiescent fluid, with the observer stationary,

$$S = [\beta^2(r^2 + r_1^2 - 2rr_1\cos(\theta - \theta_1)) + (z - cM_\infty t)^2]^{1/2}, \tag{3a}$$

$$\sigma = (S + M_\infty z)/\beta^2, \tag{3b}$$

$$\beta = (1 - M_\infty^2)^{1/2}.$$

and when the propeller and observer are both stationary in a uniform flow,

$$S = [\beta^2(r^2 + r_1^2 - 2rr_1\cos(\theta - \theta_1)) + z^2]^{1/2}, \tag{4a}$$

$$\sigma = (S + M_\infty z)/\beta^2. \tag{4b}$$

In the moving propeller case, co-ordinates are chosen such that the propeller axial displacement is given by $z = cM_\infty t$.

2.1. ACOUSTIC PRESSURE

The solution of equation (1) is given by the Ffowcs Williams–Hawkings equations [1, 2, 15] as an integral over the source surface:

$$p(\mathbf{x}, t) = \frac{\mathrm{D}}{\mathrm{D}t}\int_A G(\mathbf{x}, t; \mathbf{y}, \tau)\rho v_n \,\mathrm{d}A - \nabla\cdot\int_A G(\mathbf{x}, t; \mathbf{y}, \tau)\,\mathbf{1}\,\mathrm{d}A, \tag{5}$$

with $G(\mathbf{x}, t; \mathbf{y}, \tau)$ denoting the Green's function for observer position and time $\mathbf{x}$ and t and source position and time $\mathbf{y}$ and τ.

Inserting the Green's function, equation (2), and noting that all quantities vary as $\exp(-\mathrm{j}n\Omega t)$, the sound radiated by the nth thickness and thrust modes is

$$p_T = -\varepsilon n^2 M_t^2 I,$$

$$I = \int_0^{2\pi}\int_0^1 f_n(r_1)\frac{\mathrm{e}^{\mathrm{j}(k\sigma + n\theta - n\theta_1)}}{2\pi S^3}\left(S\sigma + \mathrm{j}\frac{M_\infty}{M_t}\frac{z}{n}\right) r_1\,\mathrm{d}r_1\,\mathrm{d}\theta_1, \tag{6}$$

$$p_L = L,$$

$$L = \int_0^{2\pi}\int_0^1 g_n(r_1)\frac{\mathrm{e}^{\mathrm{j}(k\sigma + n\theta - n\theta_1)}}{4\pi S^3}\left(z - \mathrm{j}\frac{kS}{\beta^2}(z + M_\infty S)\right) r_1\,\mathrm{d}r_1\,\mathrm{d}\theta_1, \tag{7}$$

where θ_1 has been transformed to $\theta - \theta_1$ with the corresponding change in the amplitude radius

$$S = [\beta^2(r^2 + r_1^2 - 2rr_1\cos\theta_1) + (z - cM_\infty t)^2]^{1/2} \quad \text{(stationary fluid)},$$

$$S = [\beta^2(r^2 + r_1^2 - 2rr_1\cos\theta_1) + z^2]^{1/2} \quad \text{(moving fluid)}.$$

The integrals have been non-dimensionalized by scaling lengths on the propeller radius a and pressures on ρc^2. In the moving propeller case, the integral is calculated at time $t = 0$, at which time, the disc is passing through $z = 0$. This makes the integrals identical in each of the two possible cases to be calculated. The result for loading noise is identical to that of Garrick and Watkins [16] except that the complex conjugate must be taken.

3. NUMERICAL METHOD FOR ACOUSTIC CALCULATIONS

To examine the properties of the whole acoustic field, the integrals of the previous section must be calculated for a large number of points to cover a region of interest at adequate resolution. Direct numerical evaluation of the two-dimensional integrals would take an unreasonably long time but the method of Chapman [13], which renders the integrals one-dimensional by a change of co-ordinate system, makes the calculation feasible.

3.1. REDUCTION TO ONE-DIMENSIONAL INTEGRALS

In a study of the acoustic field radiated by a stationary propeller, Chapman introduces a technique for the reduction of the two-dimensional radiation integrals to single integrals in a new co-ordinate system. The integrals are transformed from the (r_1, θ_1) co-ordinate system to the new system (r_2, θ_2) (Figure 2). The co-ordinates are based on lines parallel to the propeller axis at a distance r, the "sidelines" of propeller noise measurements. From Figure 2,

$$r_1^2 = r^2 + r_2^2 + 2rr_2 \cos\theta_2, \tag{8}$$

$$\tan\theta_1 = \frac{r_2 \sin\theta_2}{r + r_2 \cos\theta_2}, \tag{9}$$

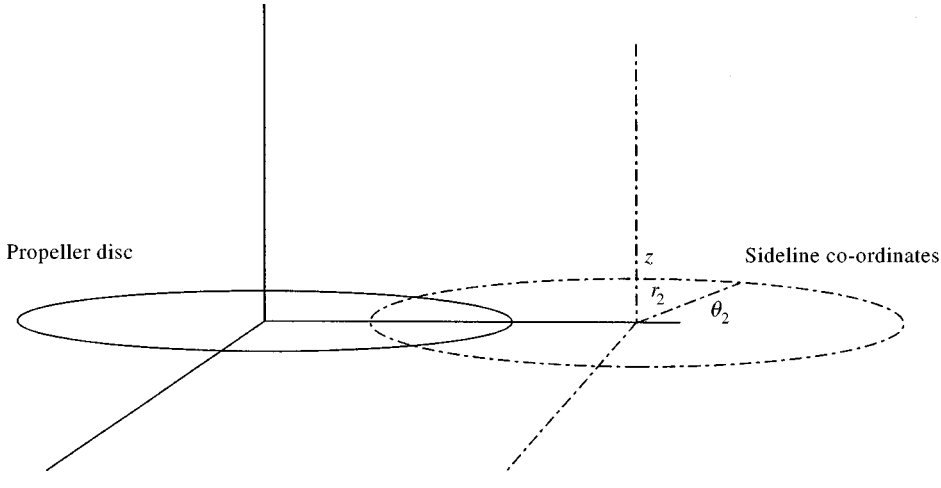

Figure 2. The new co-ordinate system for integration.

so that

$$r_1 \, dr_1 \, d\theta_1 = r_2 \, dr_2 \, d\theta_2. \tag{10}$$

Taking the thickness noise term as an example, this gives a new integral,

$$I = \int_{\max(0, r-1)}^{r+1} \frac{e^{j(k\sigma + n\theta)}}{S^3} \left(S\sigma + j \frac{M_\infty}{M_t} \frac{z}{n} \right) J(r, r_2) r_2 \, dr_2, \tag{11}$$

$$J(r, r_2) = \frac{1}{2\pi} \int_{\theta_2} f_n(r_1) e^{-jn\theta_1} \, d\theta_2. \tag{12}$$

In the evaluation of J, the limits of integration are determined by the intersection of a circle of radius r_2 with the propeller disc (Figure 3). There are five distinct possibilities for this intersection, of which one is the trivial case where the circle of radius r_2 does not contact the propeller disc. The remaining four cases are listed by Chapman [13] and are shown in Figure 4.

For certain forms for $f_n(r_1)$, the integral for J can be evaluated analytically and only a one-dimensional integral need be performed numerically. In reference [13] $f_n \equiv 1$ and the calculation is performed for the case with no mean flow, with a recursive formula being given for J. In the case of a system with an axial mean flow, an identical method can be used. In the next sections, formulae for J are derived which allow a polynomial representation of f_n.

3.2. INTEGRAL REPRESENTATION FOR J

The starting point for the formulae for J is a complex integral representation derived by combining expressions for $\exp(jn\theta_1)$ and r_1^2 written as functions of

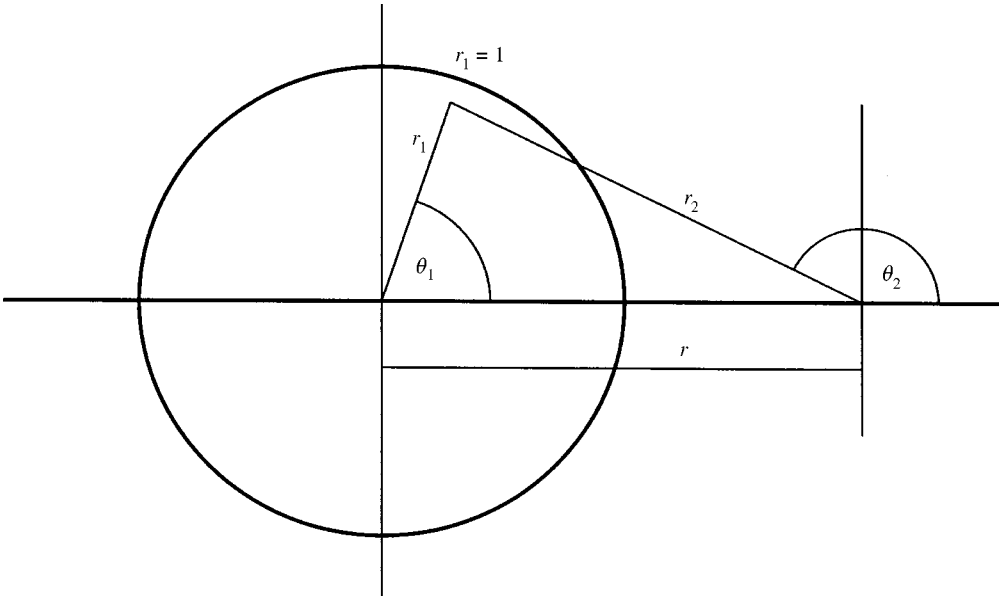

Figure 3. Sideline co-ordinate transformation.

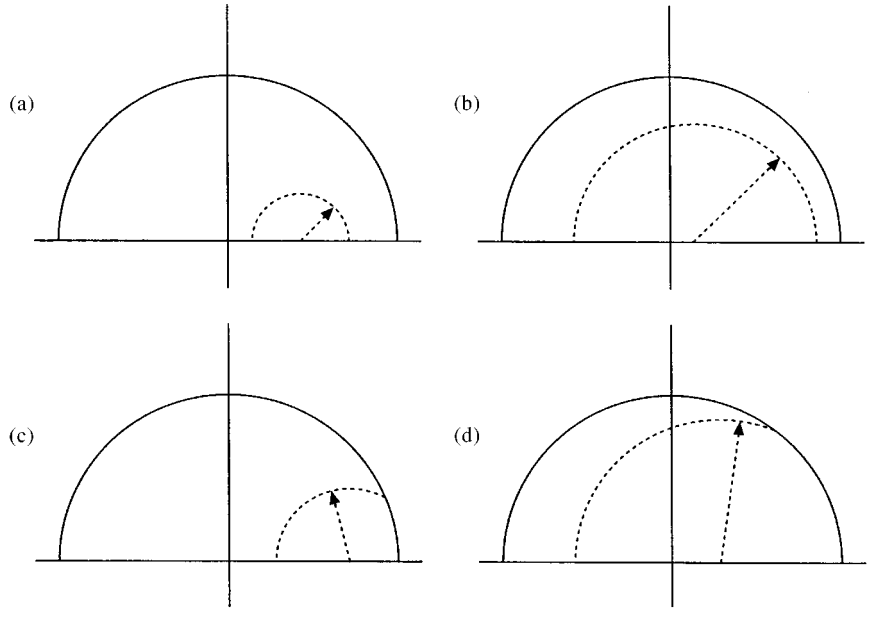

Figure 4. Different cases for determination of limits in integral representation of J. The limits are determined by the intersection of a circle of radius r_2 (shown dashed) with a circle of radius $r_1 = 1$. (a) $r > 1/2$, $r_2 < 1 - r$; (b) $r < 1/2$, $r < r_2 < 1 - r$; (c) $r > 1/2$, $1 - r < r_2 < r$; (d) $r_2 > r$.

θ_2 and r_2. From Figure 3.

$$r_1 e^{-j\theta_1} = \frac{r}{\mu}(\mu + r_2/r), \tag{13}$$

and

$$r_1^2 = \frac{r r_2}{\mu}(\mu + r/r_2)(\mu + r_2/r) \tag{14}$$

with

$$\mu \equiv e^{j\theta_2}.$$

These expressions allow an integral expression for J to be written for a source distribution whose radial variation is expressed in even or odd powers of r_1, for even and odd harmonic numbers respectively. For this purpose a modified notation is introduced. The function J is replaced by a sum of functions $J_{n,p}$ where $J_{n,p}(r, r_2)$ is used to calculate the noise radiated by an acoustic mode of strength $r_1^p \exp(-jn\theta_1)$.

In the following sections, integral formulations for the odd and even harmonic cases are given and are then used to develop exact, finite series, representations for the radiation functions in section 3.3. For numerical reasons, an infinite series form is also derived in section 3.4.

For $n = 2m$, note that

$$r_1^{2q} e^{-j2m\theta_1} = (r_1 e^{-j\theta_1})^{2m} (r_1^2)^{q-m}$$

and from equation (13) and (14) one can immediately write the integral expression

$$J_{2m,2q}(r,r_2)=\frac{1}{2\pi}\int_{\theta_2^{(0)}}^{2\pi-\theta_2^{(0)}} r_1^{2q}\mathrm{e}^{-\mathrm{j}2m\theta_1}\,\mathrm{d}\theta_2,$$

$$=r^{2q}t^{q-m}\frac{1}{\mathrm{j}2\pi}\int_{\mu_0}^{\mu_0^*}\frac{(\mu+t)^{m+q}}{(\mu+\eta)^{m-q}}\frac{1}{\mu^{m+q+1}}\,\mathrm{d}\mu, \tag{15}$$

where

$$\mu_0=\mathrm{e}^{\mathrm{j}\theta_2^{(0)}},\qquad \theta_2^{(0)}=\cos^{-1}\frac{1-r^2-r_2^2}{2rr_2},$$

$$t=r_2/r\quad\text{and}\quad\eta=r/r_2.$$

The cases of most interest for the evaluation of $J_{2m,2q}$ are those where $q>0$. Of particular interest are those cases for $q<m$, the lower-order terms in a series representation of the radial source variation.

Proceeding in the same manner as above, for $n=2m+1$ and for a series of terms r_1^{2q+1}, the integral representation for $J_{2m+1,2q+1}$ is written

$$J_{2m+1,2q+1}(r,r_2)=r^{2q+1}t^{q-m}\frac{1}{\mathrm{j}2\pi}\int_{\mu_0}^{\mu_0^*}\frac{(\mu+t)^{m+q+1}}{(\mu+\eta)^{m-q}}\frac{1}{\mu^{m+q+2}}\,\mathrm{d}\mu \tag{16}$$

For completeness, we also give the form of integrals for $J_{n,p}$ when n and p are not both odd or both even:

$$J_{2m+1,2q}(r,r_2)=r^{2q}t^{q-m-1/2}\frac{1}{\mathrm{j}2\pi}\int_{\mu_0}^{\mu_0^*}\frac{(\mu+t)^{m+q+1/2}}{(\mu+\eta)^{m-q+1/2}}\frac{1}{\mu^{m+q+1/2}}\,\mathrm{d}\mu \tag{17}$$

$$J_{2m,2q+1}(r,r_2)=r^{2q+1}t^{q-m+1/2}\frac{1}{\mathrm{j}2\pi}\int_{\mu_0}^{\mu_0^*}\frac{(\mu+t)^{m+q+1/2}}{(\mu+\eta)^{m-q-1/2}}\frac{1}{\mu^{m+q+3/2}}\,\mathrm{d}\mu \tag{18}$$

These integrals do not have the convenient closed-form solutions of $J_{2m,2p}$ and $J_{2m+1,2p+1}$ but can be evaluated as infinite series using the methods of section 3.4. Since they will not be used for the acoustic field calculations of this paper, they will not be considered further.

3.3. FINITE SERIES FOR $J_{n,p}$

The integral representations for $J_{n,p}$ given in equations (15) and (16) can be used to derive exact formulae for the radiation functions. The case of even harmonic number with $q<m$ is considered first. Expanding equation (15),

$$J_{2m,2q}=r^{2q}t^{q-m}\sum_{k=0}^{m+q}\binom{m+q}{k}t^k\int_{\mu_0}^{\mu_0^*}\frac{1}{\mu^{k+1}}\frac{1}{(\mu+\eta)^{m-q}}\,\mathrm{d}\mu. \tag{19}$$

The integrands in this equation have a partial series expansion [17],

$$\frac{1}{\mu^{k+1}}\frac{1}{(\mu+\eta)^{m-q}} = \sum_{i=1}^{k+1}\frac{A_i(t)}{\mu^i} + \sum_{i=1}^{m-q}\frac{B_i(t)}{(\mu+\eta)^i}, \tag{20}$$

with A_i and B_i given by

$$A_i = \frac{1}{(k+1-i)!}\lim_{\mu\to 0}\frac{\mathrm{d}^{k+1-i}}{\mathrm{d}\mu^{k+1-i}}\frac{1}{(\mu+\eta)^{m-q}},$$

$$B_i = \frac{1}{(m-q-i)!}\lim_{\mu\to -\eta}\frac{\mathrm{d}^{m-q-i}}{\mathrm{d}\mu^{m-q-i}}\frac{1}{\mu^{k+1}}.$$

Then,

$$A_i = -(-)^{k-i}\binom{m-q+k-i}{m-q-1}t^{m-q+k+1-i} \tag{21}$$

$$B_i = (-)^{k+i}\binom{m-q+k-i}{m-q-i}t^{m-q+k+1-i} \tag{22}$$

so that

$$J_{n,q} = r^{2q}\sum_{k=0}^{m+q}\binom{m+q}{k}(-t^2)^k\sum_{i=1}^{k+1}\binom{m-q+k-i}{m-q-1}(-t)^{1-i}\frac{1}{\mathrm{j}2\pi}\int_{\mu_0}^{\mu_0^*}\frac{1}{\mu^i}\,\mathrm{d}\mu$$

$$-r^{2q}\sum_{k=0}^{m+q}\binom{m+q}{k}(-t^2)^k\sum_{i=1}^{m-q}\binom{m-q+k-i}{m-q-i}t^{1-i}\frac{1}{\mathrm{j}2\pi}\int_{\mu_0}^{\mu_0^*}\frac{1}{(\mu+\eta)^i}\,\mathrm{d}\mu$$

Evaluating the integrals in μ, this becomes

$$J_{2m,2q} = -\frac{r^{2q}}{\pi}\sum_{k=0}^{m+q}\binom{m+q}{k}(-t^2)^k\sum_{i=1}^{k+1}\binom{m-q+k-i}{m-q-1}(-t)^{1-i}\frac{\sin(1-i)\theta_2^{(0)}}{1-i}$$

$$+\frac{r^{2q}}{\pi}\sum_{k=0}^{m+q}\binom{m+q}{k}(-t^2)^k\sum_{i=1}^{m-q}\binom{m-q+k-i}{m-q-i}(1/r)^{1-i}\frac{\sin(1-i)\alpha}{(1-i)} \tag{23}$$

with

$$\alpha = \tan^{-1}\frac{\sin\theta_2^{(0)}}{\eta+\cos\theta_2^{(0)}}.$$

For $i=1$ in the summations,

$$\frac{\sin(1-i)\theta_2^{(0)}}{(1-i)} \text{ is replaced by } \theta_2^{(0)}-\pi \tag{24}$$

and

$$\frac{\sin(1-i)\alpha}{(1-i)} \text{ is replaced by } \begin{cases} \alpha, & t \leqslant 1, \\ \alpha - \pi & t > 1. \end{cases} \tag{25}$$

When $q \geqslant m$, the formula for $J_{2m,2q}$ is somewhat less involved,

$$\begin{aligned} J_{2m,2q} &= r^{2q} t^{q-m} \frac{1}{\mathrm{j}2\pi} \int_{\mu_0}^{\mu_0^*} (\mu + t)^{q+m} (\mu + \eta)^{q-m} / \mu^{q+m+1} \, \mathrm{d}\mu, \\ &= r^{2q} \sum_{k=0}^{q+m} \sum_{i=0}^{q-m} \binom{q+m}{k} \binom{q-m}{i} t^{k+i} \frac{1}{\mathrm{j}2\pi} \int_{\mu_0}^{\mu_0^*} \frac{1}{\mu^{k-i+1}} \, \mathrm{d}\mu \\ &= -\frac{r^{2q}}{\pi} \sum_{k=0}^{q+m} \sum_{i=0}^{q-m} \binom{q+m}{k} \binom{q-m}{i} t^{k+i} \frac{\sin(k-i+1)\theta_2^{(0)}}{(k-i+1)}. \end{aligned} \tag{26}$$

The same procedure can be carried out for n odd, giving, for $q < m$.

$$\begin{aligned} J_{2m+1,2q+1} = & \\ & -\frac{r^{2q+1}}{\pi} \sum_{k=0}^{m+q+1} \binom{m+q+1}{k} (-t^2)^k \sum_{i=1}^{k+1} \binom{m-q+k-i}{m-q-1} (-t)^{1-i} \frac{\sin(1-i)\theta_2^{(0)}}{(1-i)} \\ & +\frac{r^{2q+1}}{\pi} \sum_{k=0}^{m+q+1} \binom{m+q+1}{k} (-t^2)^k \sum_{i=1}^{m-q} \binom{m-q+k-i}{m-q-i} (1/r)^{1-i} \frac{\sin(1-i)\alpha}{(1-i)} \end{aligned} \tag{27}$$

and for $q \geqslant m$,

$$J_{2m,2q+1} = -\frac{r^{2q+1}}{\pi} \sum_{k=0}^{q+m+1} \sum_{i=0}^{q-m} \binom{q+m+1}{k} \binom{q-m}{i} t^{k+i} \frac{\sin(k-i+1)\theta_2^{(0)}}{(k-i+1)}. \tag{28}$$

At this stage, the radiated harmonic strength, for n odd or even and with a source distribution expressed in a series of odd or even powers of r_1, can be calculated using the definitions of $J_{n,p}$ given in this section. There is, however, a numerical difficulty associated with the calculation of $J_{n,p}$ when t is large, i.e. when the observer position is very close to the propeller axis. This can be avoided using an expansion of $J_{n,p}$ in an infinite series in η.

3.4. INFINITE SERIES FOR $J_{n,p}$

When $r \ll 1$, the finite series formulae for $J_{n,p}$ may not give the correct answer due to numerical errors in calculating the difference between large powers of $t = r_2/r$. To work around this problem, an expansion of $J_{n,p}$ in powers of η (i.e. inverse powers of t) is used.

For n even and $q < m$, using Leibnitz' rule for differentiation of a product [18],

$$J_{2m,2q} = \frac{r^{2q}t^{2q}}{j2\pi}\int_{\mu_0}^{\mu_0^*}\frac{(1/\mu+\eta)^{m+q}}{(\mu+\eta)^{m-q}}\frac{1}{\mu}\,d\mu,$$

$$= r^{2q}t^{2q}\sum_{k=0}^{\infty}\frac{\eta^k}{k!}\frac{1}{2\pi}\int_{\mu_0}^{\mu_0^*}\frac{d^k}{d\eta^k}\frac{(1/\mu+\eta)^{m+q}}{(\mu+\eta)^{m-q}}\frac{1}{\mu}\bigg|_{\eta=0}d\mu,$$

$$= -\frac{r^{2q}t^{2q}}{\pi}\sum_{k=0}^{\infty}\eta^k\sum_{i=\max(0,k-m-q)}^{k}(-)^i\binom{m-q+i-1}{m-q-1}$$

$$\times\binom{m+q}{k-i}\frac{\sin(2m+2i-k)\theta_2^{(0)}}{(2m+2i-k)},$$

which can be rewritten

$$= -\frac{r^{2q}t^{2q}}{\pi}\sum_{i=0}^{\infty}\binom{m-q+i-1}{m-q-1}(-\eta)^i$$

$$\times\sum_{k=0}^{k=m+q}\binom{m+q}{k}\frac{\sin(2m+i-k)\theta_2^{(0)}}{(2m+i-k)}\eta^k. \tag{29}$$

This series converges for small η (large t) and, more importantly, is not subject to the numerical difficulties involved in calculating $J_{2m,2q}$ directly from the formulae of the previous sections. Finally, for n odd,

$$J_{2m+1,2q+1} = -\frac{r^{2q+1}t^{2q+1}}{\pi}\sum_{i=0}^{\infty}\binom{m-q+i-1}{m-q-1}(-\eta)^i$$

$$\times\sum_{k=0}^{k=m+q+1}\binom{m+q+1}{k}\frac{\sin(2m+i-k+1)\theta_2^{(0)}}{(2m+i-k+1)}\eta^k. \tag{30}$$

3.5. CASES 1 AND 2

An 'intriguing' result of Chapman's paper [13] is that for case 2 of Figure 3, $J \equiv 0$. This result can be recovered from the integral representation of $J_{n,q}$, (15). For cases 1 and 2 of Figure 3, the contour of integration is the whole unit circle,

$$J_{2m,2q} = r^{2q}t^{q-m}\frac{1}{j2\pi}\oint_{|\mu|=1}\frac{(\mu+t)^{m+q}}{(\mu+\eta)^{m-q}}\frac{1}{\mu^{m+q+1}}\,d\mu. \tag{31}$$

There are two possible singularities within the contour of integration, at the origin and at $\mu = -\eta$. The case when the origin is the only singularity corresponds to

case 1 of Figure 3. Case 2 corresponds to $\eta < 1$ (i.e., $t > 1$). For $q < -m$, the singularity at the origin disappears and $J_{n,q} \equiv 0$ for case 1. In case 2, when $-m \leqslant q < m$, the value of the integral is given by the sum of the residues at the singularities. These can be found from the partial fraction expansion given above with only A_1 and B_1 from equations (21) and (22) required. Then, since $A_1 \equiv -B_1$, the integral is identically equal to zero, reproducing and extending Chapman's previous result. When $q \geqslant m$, only the singularity at the origin remains and the integral is finite in both cases 1 and 2.

4. RESULTS

Programs have been written to evaluate equations (6) and (7) for a range of tip and inflow Mach numbers. Two basic test cases have been chosen, for propellers of tip speed $M_t = 0{\cdot}7$ and $1{\cdot}05$. These parameters roughly represent a "conventional" and an "advanced" propeller. Flight Mach numbers $M_\infty = 0, 0{\cdot}2$ were chosen for both propellers ($0{\cdot}2$ being a reasonable figure for takeoff) and $M_\infty = 0{\cdot}7$ for the conventional propeller and $M_\infty = 0{\cdot}8$ for the advanced. The acoustic field was calculated in each case over the region $0 \leqslant r \leqslant 3$, $-3 \leqslant z \leqslant 3$. The harmonic number was set to $n = 16$ for comparison with Chapman's stationary disc results [13] and the thickness and loading terms were assumed independent of radius under all operating conditions.

4.1. NUMERICAL METHOD

A simple program was written to evaluate the function $J_{n,p}$ of section 3 for use in the integration of equations (32) and (33). The calculated values of $J_{n,0}$ were checked against results from Chapman's method [13] and values for general p were tested against direct numerical integration of equation (15).

After transformation to (r_2, θ_2) co-ordinates, equations (6) and (7) become

$$I = \int_{r_2} \frac{e^{j(k\sigma + n\theta)}}{S^3} \left(S\sigma + j \frac{M_\infty}{M_t} \frac{z}{n} \right) J_{n,0}(r, r_2) r_2 \, dr_2, \tag{32}$$

$$L = \frac{1}{2} \int_{r_2} \frac{e^{j(k\sigma + n\theta)}}{S^3} \left(z - j \frac{kS}{\beta^2} (z + M_\infty S) \right) J_{n,0}(r, r_2) r_2 \, dr_2, \tag{33}$$

with

$$S = (\beta^2 r_2^2 + z^2)^{1/2}.$$

At this point, the physical reason for the efficiency of the adopted procedure can be noted. The new co-ordinate system (r_2, θ_2) is one in which all points at a given r_2 are also at the same phase and amplitude radius from the observation point. In effect, the integration in θ_2 gathers the contribution from each point at a given value of S and σ and the integration in r_2 collects the individual contributions to the overall integral.

The sound fields were calculated on a meridional grid of 201 points in r and 402 points in z. In integrating equations (32) and (33) it was possible to calculate the acoustic field for all six operating conditions simultaneously. The method adopted was to fix the value of r and then calculate $J_{n,0}(r, r_2)$, r_2 being sampled over the relevant range of integration. This was then stored for reuse at each value of z at the given value of r and at each of the six operating conditions. In this manner, it was possible to calculate the $6 \times 80\,802$ field points in about 16 h of real time (i.e., not CPU time) on a personal computer. The calculated field data were then spot-checked by calculating the harmonic strength at selected points using a full two-dimensional integration.

4.2. ACOUSTIC FIELDS

The two sets of data (thickness and loading) have been plotted in Figures 5–8 on two different sections through the acoustic field, one across the propeller axis at $z = 0$ (thickness) or $z = 0{\cdot}1$ (loading), the other a meridional section $\theta = 0$. In each case, the real part of the integral is plotted, this corresponding to the instantaneous acoustic pressure due to the source harmonic under consideration. Due to the large variation in field strength, logarithmically spaced values have been chosen for the contours. Negative values have been omitted from Figures 5 and 6 as they can be recovered by rotation through π/n radians. In the meridional plots, Figures 7 and 8, the negative contours are shown as dashed lines.

Looking first at the thickness noise of the subsonic tip speed propeller [Figures 5(a–c) and 7(a–c)], the form of the sound field for $M_\infty = 0$ is the same as that for reference [13]; the near field is made up of alternating regions of positive and negative pressure forming segments of an "orange" which undergoes a transition into the farfield radiation zone with its spiral bands clearly visible in Figure 5(a). As in previously published results, the wavelength in the far field is $2\pi/M_t n$. The transition from the near to the far field begins at the sonic radius $1/M_t$ and is completed half an acoustic wavelength further out, in agreement with the definition of reference [13] where the radiation zone is taken as beginning a quarter wavelength inboard of the $I = 0$ contour. The physical structure of the field is one of a near field which allows a small amount of radiation to 'leak' into the far field across the curved boundary. The object of this paper is to examine how this acoustic field develops as a mean flow is applied to the system.

Figures 5(b) and 7(b) show the effect of adding a mean flow of $M_\infty = 0{\cdot}2$, a typical take-off condition. The flow in each case is from right to left in the meridional plane or, alternatively, the propeller moves from left to right relative to a stationary observer. The first point to note is that the $z = 0$ section has hardly changed. The blade-tip helical Mach number is now 0·73 so that the sonic radius has moved inboard to 1·40 but remains outside the propeller disc. The whole propeller is still inside the near field and the acoustic energy must still tunnel across the far field boundary. The meridional section on the other hand shows a marked alternation. The nearfield boundary has been squashed against the front of the disc and stretched out behind it, a trend which continues as the inflow Mach number is increased to 0·7.

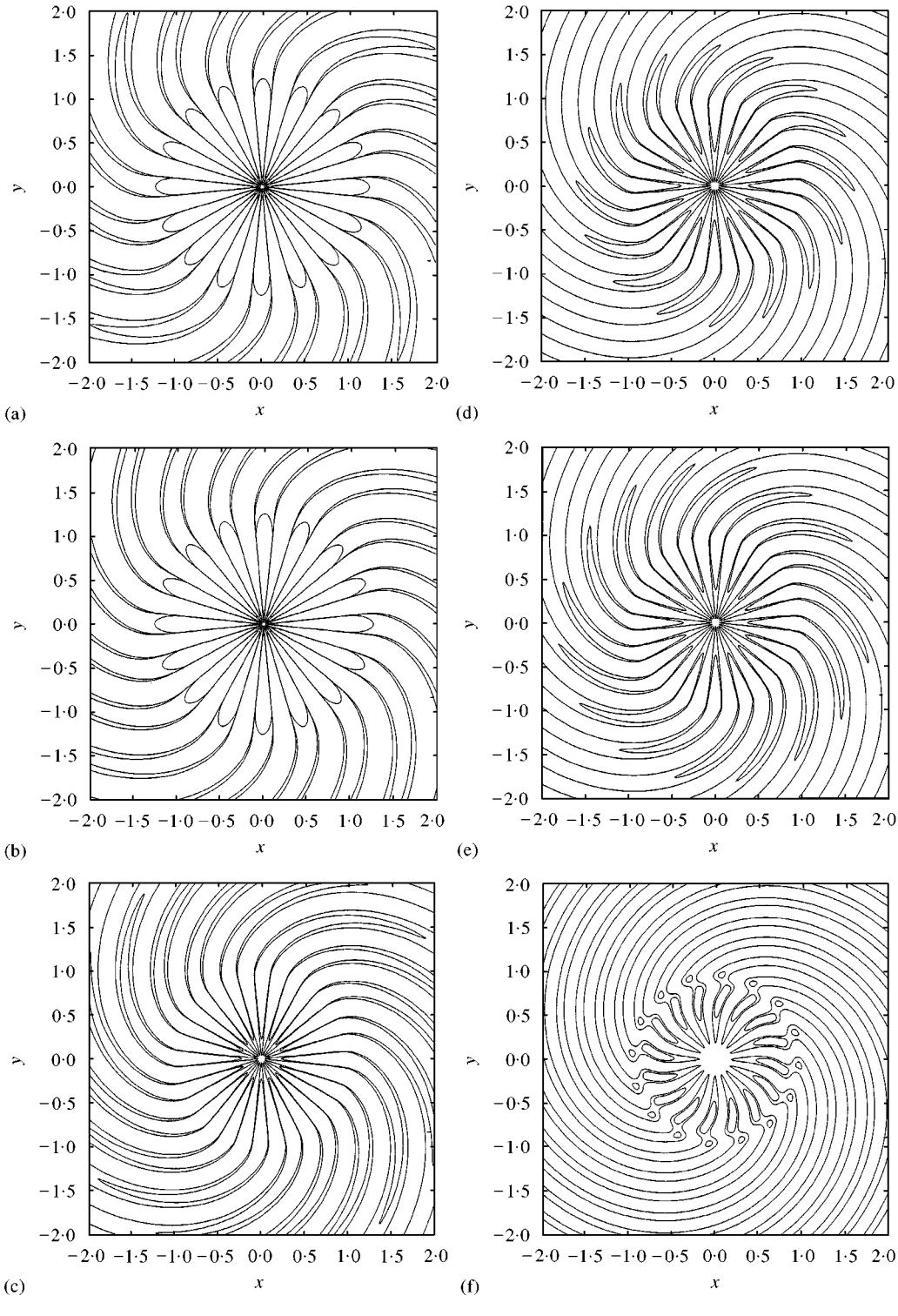

Figure 5. Thickness noise fields, $z = 0$. (a) $M_t = 0{\cdot}7$, $M_\infty = 0$, contour levels 10^{-5}, 10^{-4}, 10^{-3}; (b) $M_t = 0{\cdot}7$, $M_\infty = 0{\cdot}2$, contour levels 10^{-5}, 10^{-4}, 10^{-3}; (c) $M_t = 0{\cdot}7$, $M_\infty = 0{\cdot}7$, contour levels 10^{-4}, 10^{-3}, 10^{-2}; (d) $M_t = 1{\cdot}05$, $M_\infty = 0$, contour levels 10^{-4}, 10^{-3}, 10^{-2}; (e) $M_t = 1{\cdot}05$, $M_\infty = 0{\cdot}2$, contour levels 10^{-4}, 10^{-3}, 10^{-2}; (f) $M_t = 1{\cdot}05$, $M_\infty = 0{\cdot}8$, contour levels 10^{-2}, 10^{-1}.

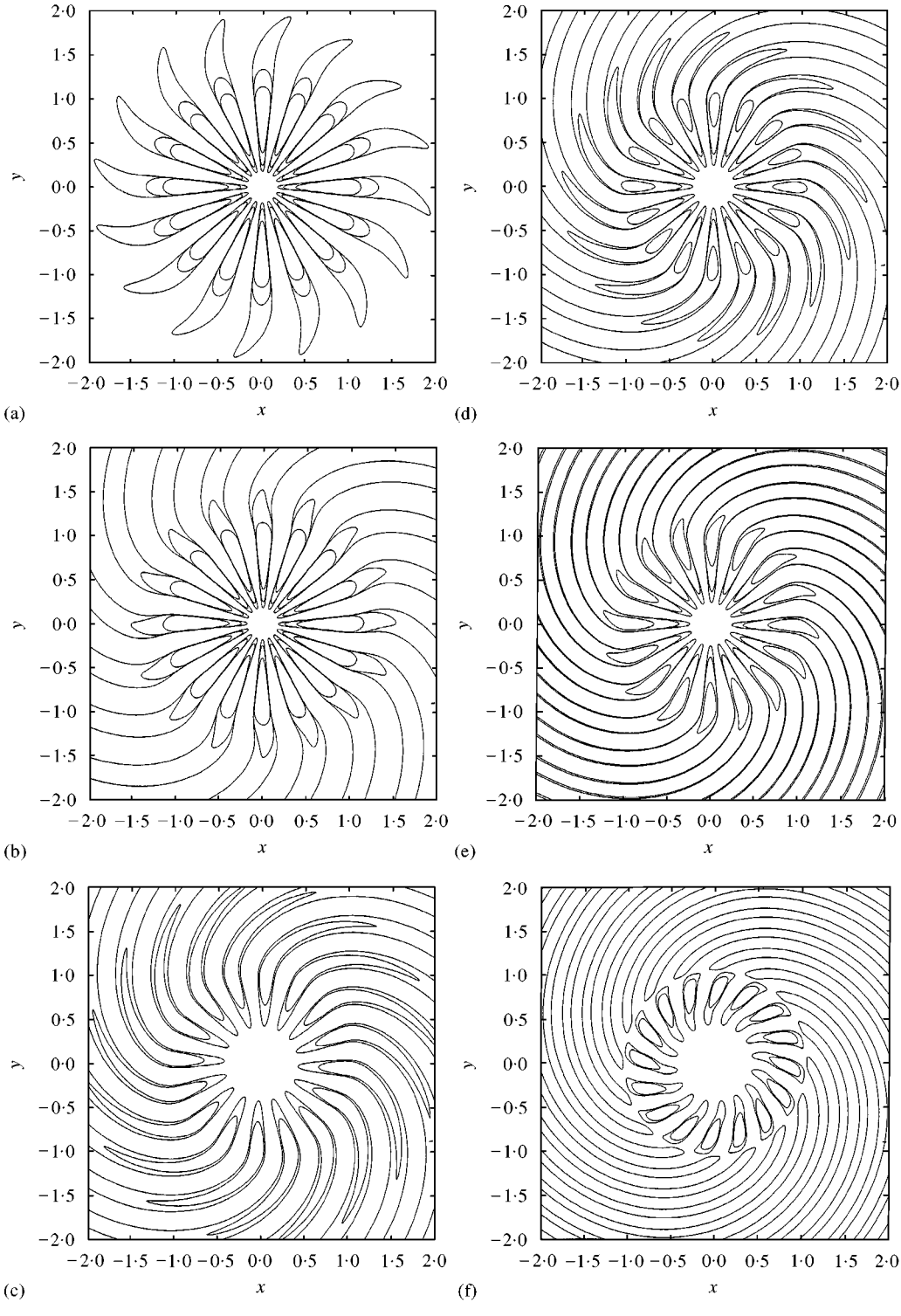

Figure 6. Loading noise fields, $z = 0{\cdot}1$. (a) $M_t = 0{\cdot}7$, $M_\infty = 0$, contour levels 10^{-4}, 10^{-3}, 10^{-2}; (b) $M_t = 0{\cdot}7$, $M_\infty = 0{\cdot}2$, contour levels 10^{-4}, 10^{-3}, 10^{-2}; (c) $M_t = 0{\cdot}7$, $M_\infty = 0{\cdot}7$, contour levels 10^{-2}, 10^{-1}; (d) $M_t = 1{\cdot}05$, $M_\infty = 0$, contour levels 10^{-3}, 10^{-2}, 10^{-1}; (e) $M_t = 1{\cdot}05$, $M_\infty = 0{\cdot}2$, contour levels 10^{-3}, 10^{-2}, 10^{-1}; (f) $M_t = 1{\cdot}05$, $M_\infty = 0{\cdot}8$, contour levels 10^{-1}, 10^{0}.

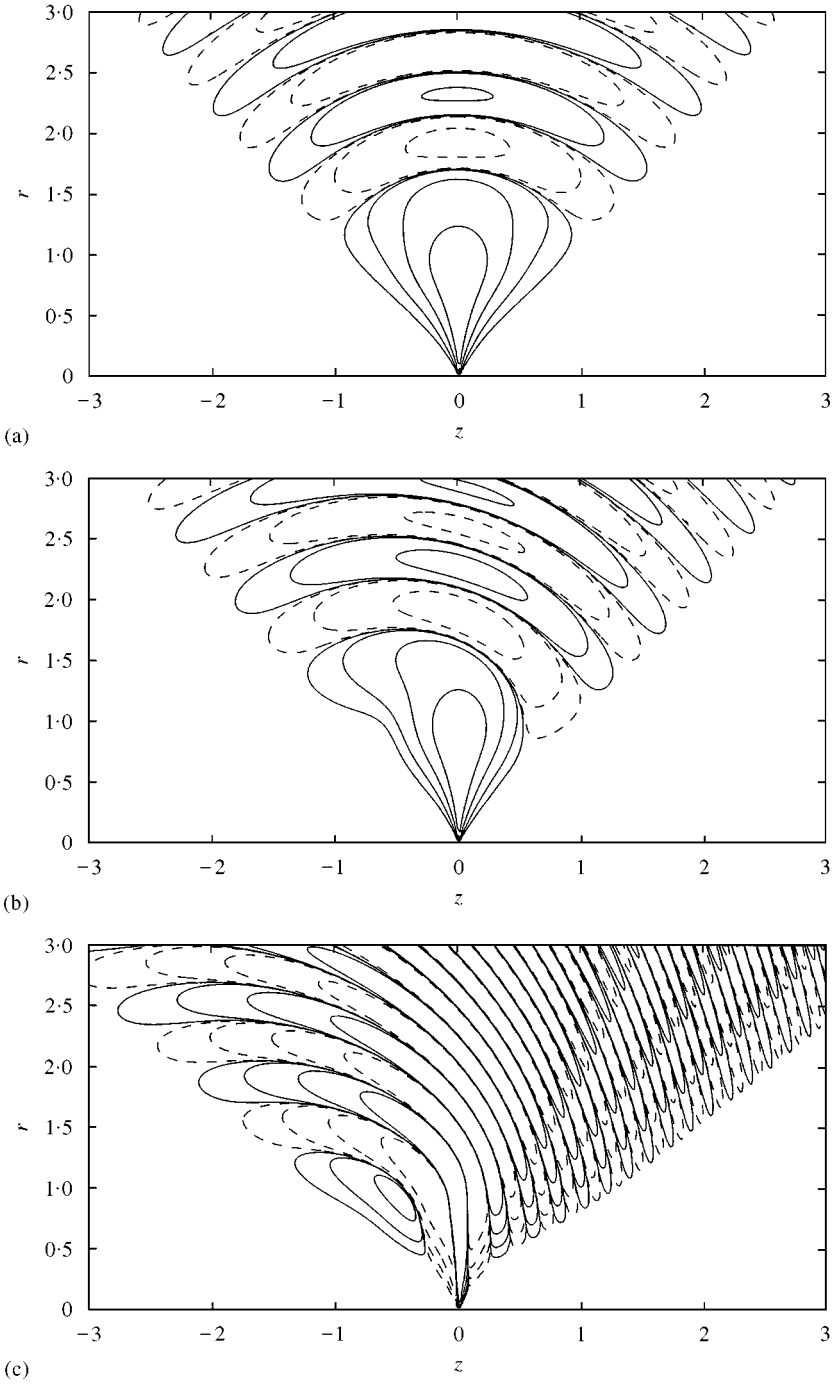

Figure 7. Thickness noise fields, $\theta = 0$. (a) $M_t = 0{\cdot}7$, $M_\infty = 0$, contour levels $\pm 10^{-6}$, $\pm 10^{-5}$, $\pm 10^{-4}$, $\pm 10^{-3}$; (b) $M_t = 0{\cdot}7$, $M_\infty = 0{\cdot}2$, contour levels $\pm 10^{-6}$, $\pm 10^{-5}$, $\pm 10^{-4}$, $\pm 10^{-3}$; (c) $M_t = 0{\cdot}7$, $M_\infty = 0{\cdot}7$, contour levels $\pm 10^{-6}$, $\pm 10^{-5}$, $\pm 10^{-4}$, $\pm 10^{-3}$; (d) $M_t = 1{\cdot}05$, $M_\infty = 0$, contour levels $\pm 10^{-5}$, $\pm 10^{-4}$, $\pm 10^{-3}$, $\pm 10^{-2}$; (e) $M_t = 1{\cdot}05$, $M_\infty = 0{\cdot}2$, contour levels $\pm 10^{-5}$, $\pm 10^{-4}$, $\pm 10^{-3}$, $\pm 10^{-2}$; (f) $M_t = 1{\cdot}05$, $M_\infty = 0{\cdot}8$, contour levels $\pm 10^{-4}$, $\pm 10^{-3}$, $\pm 10^{-2}$.

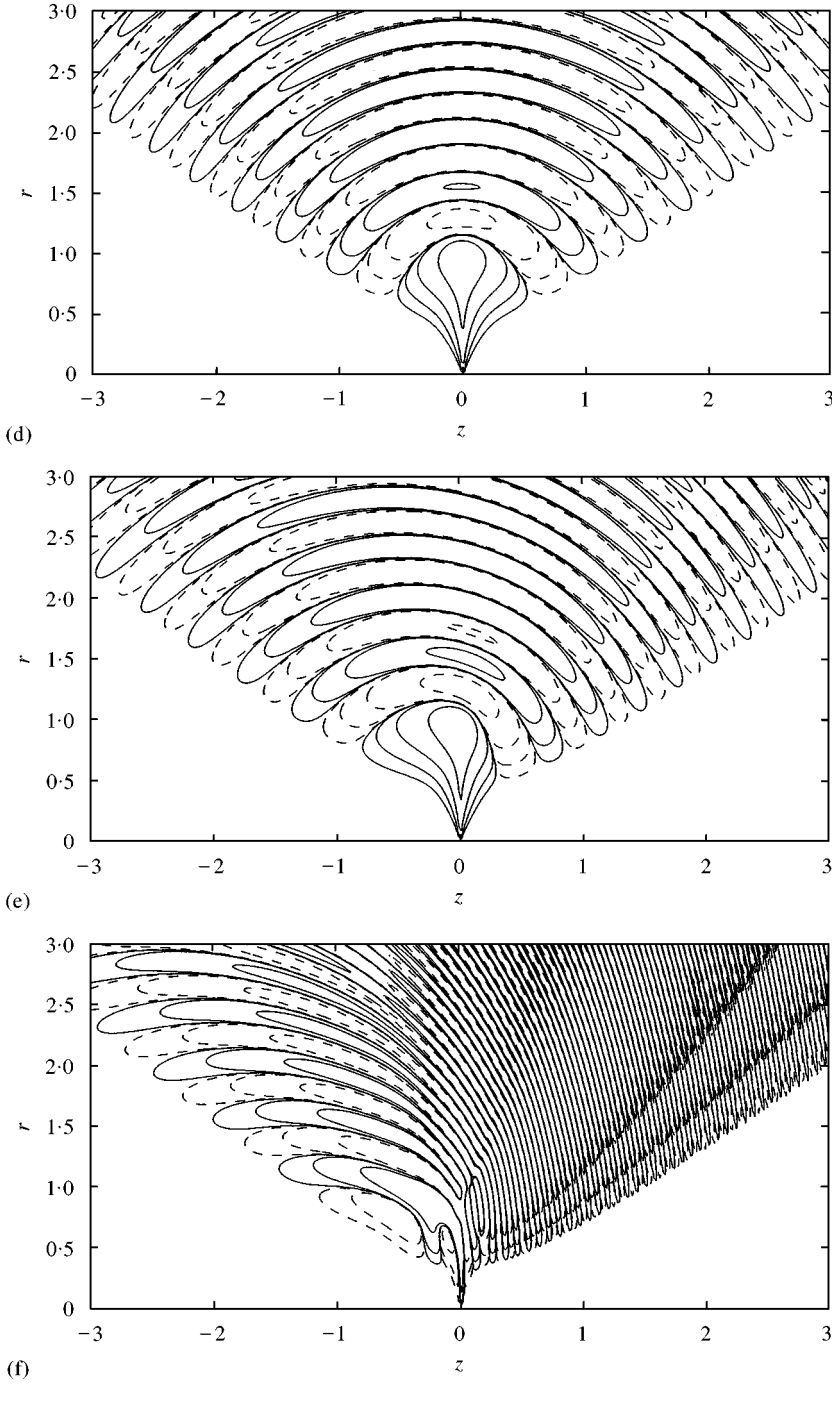

Figure 7. Continued.

Now, Figure 5(c), the tip Mach number is 0·99 and the Mach radius is at 1·02, just outside the propeller disc. The transition to the far field now occurs much closer to the propeller tip and the radiation mechanism is more efficient, less energy

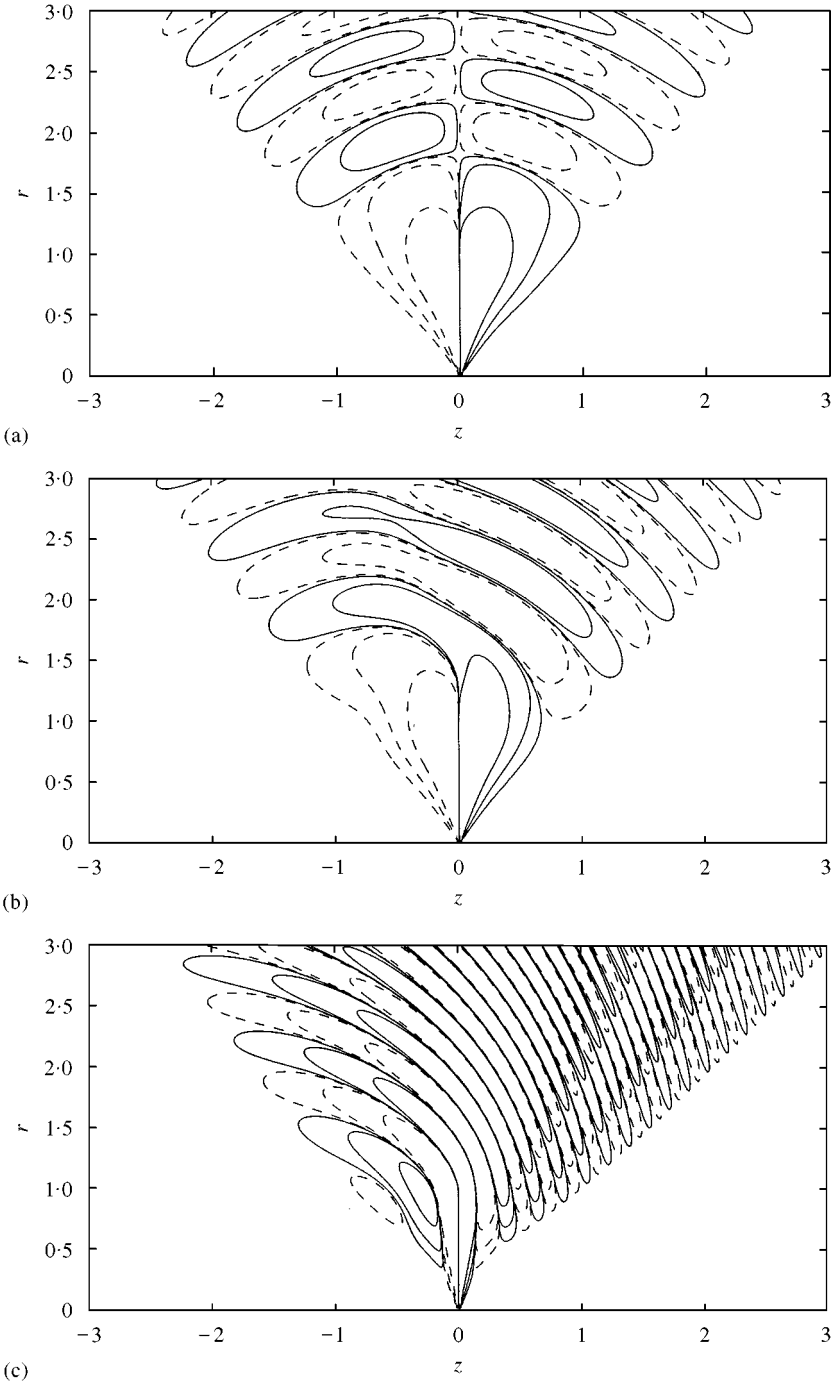

Figure 8. Loading noise fields, $\theta = 0$. (a) $M_t = 0{\cdot}7$, $M_\infty = 0$, contour levels $\pm 10^{-5}$, $\pm 10^{-4}$, $\pm 10^{-3}$; (b) $M_t = 0{\cdot}7$, $M_\infty = 0{\cdot}2$, contour levels $\pm 10^{-5}$, $\pm 10^{-4}$, $\pm 10^{-3}$; (c) $M_t = 0{\cdot}7$, $M_\infty = 0{\cdot}7$, contour levels , $\pm 10^{-4}$, $\pm 10^{-3}$, $\pm 10^{-2}$; (d) $M_t = 1{\cdot}05$, $M_\infty = 0$, contour levels $\pm 10^{-4}$, $\pm 10^{-3}$, $\pm 10^{-2}$; (e) $M_t = 1{\cdot}05$, $M_\infty = 0{\cdot}2$, contour levels $\pm 10^{-4}$, $\pm 10^{-3}$, $\pm 10^{-2}$; (f) $M_t = 1{\cdot}05$, $M_\infty = 0{\cdot}8$, contour levels $\pm 10^{-2}$, $\pm 10^{-1}$.

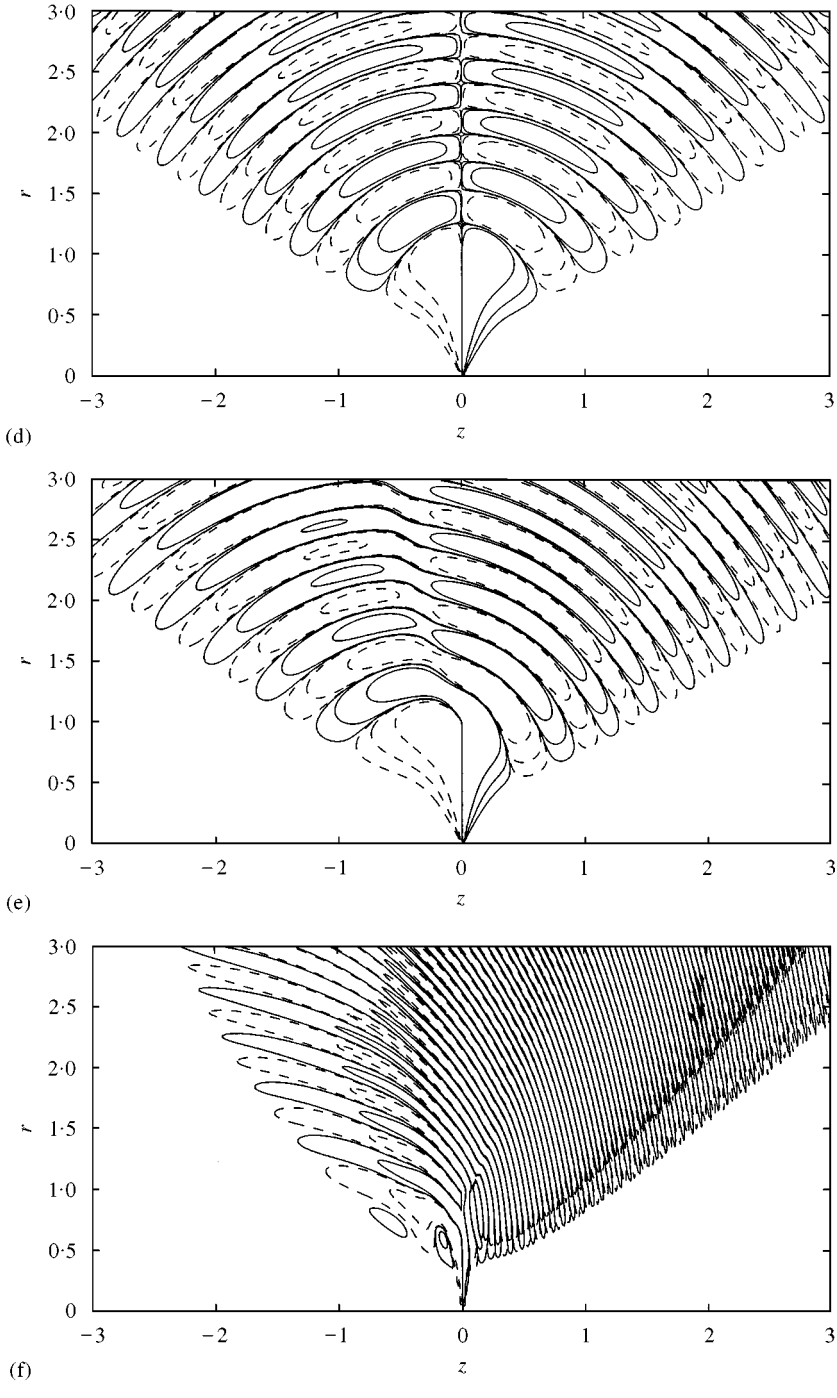

Figure 8. Continued.

being lost in "tunnelling" into the far field. The meridional section shows the distortion of the nearfield boundary with the same squashing ahead of the disc and stretching behind it. Furthermore, the farfield contours show the Doppler shifting

of the acoustic wavelength with angle from the positive z-axis, an effect not readily apparent in the $M_\infty = 0{\cdot}2$ case.

The acoustic field for the supersonic tip propeller at zero advance velocity [Figures 5(d) and 7(d)] has a similar form. The sonic radius is at $r = 0{\cdot}95$ so that the blade tips only enter the transition region between the near and far fields. The $z = 0$ section is thus quite similar to that of the cruise condition for the subsonic tip propeller. Obviously, the meridional section shows the near field boundary to be symmetric about $z = 0$ and again the far-field wavelength is $2\pi/M_t n$. At this only slightly supersonic operating condition, the strong beaming pattern characteristic of a very high tip speed rotor is not yet apparent and the radiated field is more like that of a slightly subsonic propeller. When a low forward velocity is applied [$M_\infty = 0{\cdot}2$, Figure 5(e) and 7(e)], the same alteration of the noise field occurs as in the subsonic tip speed case. The nearfield boundary is squashed against the front of the propeller disc and stretched out behind it and there is a small variation in the farfield acoustic wavelength with directivity angle. The $z = 0$ section however is quite similar to that in the no-flow case since the sonic radius is at $r = 0{\cdot}93$, less than a quarter wavelength from the propeller tip so that the whole disc still lies inside the near field.

It is only when the inflow velocity is increased to a Mach number of 0·8 that the classic "supersonic rotor" features become apparent [Figures 5(f) and 7(f)]. The sonic radius is now at $r = 0{\cdot}57$, more than an acoustic wavelength from the propeller tip, so that part of the propeller sticks out into the radiation zone. The strong beaming pattern characteristic of high-speed rotors is now obvious in the meridional section [Figure 5(f)]. The transition to the far field, the radiation zone, now begins well inside the disc radius $r = 1$ and this has a strong influence on the directivity pattern. The "orange" structure has disappeared to be replaced by a form reminiscent of that of Chapman's result for a stationary disc with $M_t = 2$.

Viewing the thickness noise figures together with those for $M_t = 2$, $M_\infty = 0$ in reference [13], it appears that the fundamental effect at work for the acoustic field characteristic of a supersonic rotor to make itself known, the propeller tip must stick out into the radiation zone with the boundary of that zone being a distance of order one wavelength past the sonic radius. The calculated sonic radius in this case includes the propeller advance velocity.

Unsurprisingly, the trends in the loading noise fields (Figures 6 and 8) follow closely those of the thickness noise data but the antisymmetry of the field about $z = 0$ in the zero-flow case allows a slightly different examination of the results. For $M_\infty = 0$, the field is zero on $z = 0$, outside the propeller disc radius. The contours have identical shapes on either side of the plane but with opposite signs. As the inflow Mach number increases, the excursions of the contours across the plane give an indication of the manner in which the field is changing. Since negative contours are shown with a different line type to positive, this is especially obvious in the contour plots.

For both tip Mach numbers, even the addition of a mean flow as slow as $M_\infty = 0{\cdot}2$ causes a large change in the meridional section [Figure 8(b, e)]. While the distortion of the contours and the nearfield boundary is the same as in the thickness noise case, the form of this distortion is highlighted. The same contour

levels have been used in Figures 8(b, e) as in (a, d) respectively to facilitate comparison. Identifying the corresponding contours in each case, the field ahead of the disc can be seen stretching backwards. Near the propeller axis, it is squashed close to the disc but at larger radii it intrudes into the negative z region. There is no corresponding excursion of the former negative z contours into the upstream zone. From the loading noise figures, the effect of the mean flow is one of stretching the acoustic field in a downstream direction.

5. CONCLUSIONS

A method has been presented for the calculation of the three-dimensional structure of the sound field around spinning sources, extending a previous analysis by Chapman [13]. For the model problem considered, the effect of the main parameters influencing the radiated noise, blade number, rotation speed and advance speed, can be studied.

The method has been applied to two sources representative of a "conventional" (subsonic) propeller and of an "advanced" (supersonic) propeller and their noise fields have been studied as functions of advance velocity which has been varied from zero to a nominal cruise condition. For the subsonic propeller, the structure of the field with an imposed flow is similar to that seen in the zero-velocity case with a near field composed of segments arranged like those of an orange and a small amount of energy tunnelling into the far field across the nearfield boundary. The main change due to the imposition of a mean flow is the alteration of the shape of the nearfield boundary which is stretched downstream, an effect most obvious in the loading noise case. The noise field of the supersonic propeller is quite similar in character to that of the subsonic propeller for the low advance Mach numbers where it does not exhibit the strong beaming of very high-speed propellers. It is only at the cruise condition that the strong directivity seen, for example, in the $M_t = 2$ case of Chapman's paper [13].

These effects can be explained in terms of the structure of the propeller near field. If the boundary of the near field is taken to be approximately one acoustic wavelength outside the sonic radius then the condition for strong radiation is that the propeller blade tips stick out into the far field. Viewing the system in terms of radiation tunnelling across the nearfield boundary, the radiated noise can be thought of in terms of the energy lost as the noise passes into the radiation zone. As the propeller Mach number, including axial motion, increases, the sonic radius reduces and the near field shrinks, For high enough tip Mach numbers, the blades penetrate the far field and no energy is lost in tunnelling, giving the strong directivity pattern characteristic of supersonic propellers. The observations of Chapman [13], based on a stationary disc model of the propeller, have been extended to the important case of a disc in a mean flow and it has been found that the same insights are valid.

REFERENCES

1. J. E. Ffowcs Williams and D. L. Hawkings 1969 *Philosophical Transactions of the Royal Society of London A* **264**, 321–342. Sound generation by turbulence and surfaces in arbitrary motion.
2. M. Goldstein 1974 *Journal of the Acoustical Society of America* **56**(2), 497–509. Unified approach to aerodynamic sound generation in the presence of solid boundaries.
3. F. Farassat 1981 *AIAA Journal* **19**, 1122–1130. Linear acoustic formulas for calculation of rotating blade noise.
4. F. Farassat 1985 In *Aerodynamics and Acoustics of Propellers*, **10**. AGARD. Theoretical analysis of linearized acoustics and aerodynamics of advanced supersonic propellers.
5. F. Farassat, M. H. Dunn and P. L. Spence 1992 *AIAA Journal* **30**, 2337–2340. Advanced propeller noise prediction in the time domain.
6. D. B. Hanson 1983 *AIAA Journal* **21**, 881–888. Compressible helicoidal surface theory for propeller aerodynamics and noise.
7. D. B. Hanson 1985 *AIAA Journal* **23**, 499–504. Near-field frequency-domain theory for propeller noise.
8. D. B. Hanson and D. J. Paryzch 1993 *NASA Contractor's Report 4499, Hamilton Standard Division, United Technologies Corporation, P.O. Box 100, Windsor Locks, Connecticut, 06096, U.S.A.* Theory for noise of propellers in angular inflow with parametric studies and experimental verification.
9. A. B. Parry and D. G. Crighton 1989 *AIAA Journal* **27**(9), 1184–2037. Asymptotic theory of propeller noise part I: Subsonic single rotation propeller.
10. D. G. Crighton and A. B. Parry 1991 *AIAA Journal* **29**(12), 2031–2037. Asymptotic theory of propeller noise part II: Supersonic single rotation propeller.
11. P. R. Prentice 1993 *Proceedings of the Royal Society of London A* **441**, 83–96. Energy transport in rotating sound fields.
12. C. J. Chapman 1992 *Proceedings of the Royal Society of London A* **436**, 511–526. The asymptotic theory of rapidly rotating sound fields.
13. C. J. Chapman 1993 *Proceedings of the Royal Society of London A* **440**, 257–271. The structure of rotating sound fields.
14. V. L. Wells and A. Y. Han 1995 *Journal of Sound and Vibration* **184**(4), 651–663. Acoustics of a moving source in a moving medium with application to propeller noise.
15. M. Carley 1996 *Ph.D. Thesis, Trinity College, Dublin, Dublin 2, Ireland.* Time domain calculation of noise generated by a propeller in a flow.
16. I. E. Garrick and C. E. Watkins 1953 *Report 1198, NACA.* A theoretical study of the effect of forward speed on the free-space sound-pressure field around propellers.
17. E. Kreyszig 1993 *Advanced Engineering Mathematics.* New York: Wiley.
18. I. Gradshteyn and I. M. Ryzhik 1980 *Table of Integrals, Series and Products* New York: Academic, fifth edition.